Geochemistry Geophysics Geosystems G3
AN ELECTRONIC JOURNAL OF THE EARTH SCIENCES
Published by AGU and the Geochemical Society

Article
Volume 3, Number 9
20 September 2002
8601, doi:10.1029/2001GC000248
ISSN: 1525-2027

Seismic anisotropy of the upper mantle 1. Factors that affect mineral texture and effective elastic properties

Donna K. Blackman
Scripps Institution of Oceanography, 8602 La Jolla Shores Drive, La Jolla, California 92037, USA (dblackman@ucsd.edu)

H.-Rudolf Wenk
Department of Earth and Planetary Sciences, University of California, Berkeley, California 94720, USA (wenk@seismo.berkeley.edu)

J. Michael Kendall
Department of Earth Sciences, University of Leeds, University of Leeds, Leeds LS2 9JT, UK (kendall@earth.leeds.ac.uk)

[1] Flow-induced mineral alignment in the Earth's mantle affects the nature of seismic wave propagation. Since measurements of seismic travel time and shear wave splitting are a key means by which the structure of the upper mantle can be imaged, it is important to understand the factors that contribute to variability in elastic properties. Seismic anisotropy associated with lattice-preferred orientations of minerals in peridotite is the focus of this study. One way to better understand anisotropy in a convecting upper mantle is to simulate texture evolution based on certain assumptions. Simulations of the development of olivine and orthopyroxene alignment along streamlines of a mantle flow field illustrate how continuously varying strain conditions affect the resulting orientation distribution. There are various uncertainties in rock texture simulations, and the aim here is to investigate how much model assumptions may influence the results. A model of upper mantle flow in the vicinity of an oceanic spreading center is used to illustrate these points. First we assess how sensitive results are on assumptions of different polycrystal plasticity models, specifically lower bounds and viscoplastic self-consistent approaches. We also investigate how recrystallization during deformation might affect the texture that develops along a streamline. The effects of grain growth and nucleation produce, as expected, textures that are different from the deformation-only case. However, the basic *P* wave structure of the predicted anisotropy is similar between models for streamlines in a slow-spreading, passive flow model as is commonly used for simulating flow near this type of plate boundary. Shear wave splitting patterns are more complex and differ somewhat more between the models in the off-axis region. We also compare predictions for texture development of olivine-only aggregates to that of mixed composition with 70% olivine and 30% orthopyroxene. Although we consider only one aspect of such polyphase deformation, i.e., plastic deformation on specified crystal slip systems, our results are consistent with field observations of the orientation distributions in ophiolitic peridotites. Finally, we determine how simplifying assumptions about the symmetry of the elastic anisotropy can bias interpretations of seismic travel time and shear wave splitting. Whereas a hexagonal approximation can lead to underestimates of the degree of anisotropy, an orthorhombic approximation is found to closely match the results predicted for a general elastic tensor corresponding to an orientation distribution whose symmetry is as low as monoclinic or triclinic.

Components: 12,919 words, 13 figures, 2 tables.

Keywords: Anisotropy; mantle convection; mineral preferred orientation; recrystallization.

Index Terms: 3902 Mineral Physics: Creep and deformation; 5120 Physical Properties of Rocks: Plasticity, diffusion, and creep; 7218 Seismology: Lithosphere and upper mantle; 8120 Tectonophysics: Dynamics of lithosphere and mantle—general.

Received 1 October 2001; **Revised** 30 April 2002; **Accepted** 10 May 2002; **Published** 20 September 2002.

Blackman, D. K., H.-R. Wenk, and J. M. Kendall, Seismic anisotropy of the upper mantle,1, Factors that affect mineral texture and effective elastic properties, *Geochem. Geophys. Geosyst.*, *3*(9), 8601, doi:10.1029/2001GC000248, 2002.

Theme: The Oman Ophiolite and Mid-Ocean Ridge Processes
Guest Editors: Peter Keleman, Chris Macleod, and Susumu Umino

1. Introduction

[2] Seismic anisotropy in the upper mantle has been linked to mineral preferred orientation (also referred to as lattice preferred orientation, LPO, or texture). Yet the relationship is very complex and depends on many aspects such as deformation history, deformation mechanisms, and local melting. For example, the mechanisms of diffusion creep, dislocation glide, and dynamic recrystallization may all contribute to the texture that occurs in a given volume of rock [*Karato and Wu*, 1993; *Zhang et al.*, 2000]. In polymineralic rocks, such as peridotite, the mechanisms controlling deformation may vary with mineral type. For example, olivine and enstatite have different slip systems, different strengths, and different shapes [*Carter*, 1976]. The fact that their single crystal elastic properties also differ means that to reliably estimate the anisotropic signature of textured peridotite in the upper mantle, the orientation distribution of both olivine and enstatite grains needs to be accounted for. Furthermore, if we model the evolution of texture and anisotropy to gain better insight into the processes, we need to make simplifications. It is necessary to evaluate which factors are most significant to produce a reliable model and which aspects are less important. For example, does the type of polycrystal plasticity model have a great influence on the results? Does the microscopic mechanism that is assumed (e.g., deformation versus recrystallization) introduce a large uncertainty?

[3] Previously we have modeled the evolution of texture along streamlines in a convecting mantle, making some arbitrary simplifying assumptions [*Chastel et al.*, 1993; *Blackman et al.*, 1996; *Dawson and Wenk*, 2000] and illustrated the dynamic nature of texture changes in an animated video [*Wenk et al.*, 1999]. In this paper we investigate how robust such conclusions about mantle seismic anisotropy are if we consider the following complicating factors: First we investigate the effect of model assumptions, particularly between a lower-bound polycrystal plasticity model and a viscoplastic self-consistent approach, on the deformation behavior of olivine. We also study the textural modifications that could be expected if dynamic recrystallization accompanies deformation. We determine the effect on elastic properties if enstatite is included as a component, in addition to olivine. Finally, we explore the influence of replacing the full elastic tensor by a high symmetry approximation, as is often used in seismology. In a companion paper we discuss textural seismic anisotropy in upper mantle flow fields for a series of plate boundary tectonic models [*Blackman and Kendall*, 2002].

[4] Our approach allows us to consider the effective elastic properties of polycrystalline rocks that undergo a strain history representative of flow fields that could reasonably occur in the Earth's mantle. The development of texture is tracked along streamlines of flow in the vicinity of an oceanic spreading center. We highlight a few

streamlines to illustrate how differences in an aggregate's strain history affect the way various factors contribute to the resulting anisotropic structure. Plate boundaries are particularly interesting regions to study seismic anisotropy, since mantle flow gradients and the corresponding degree of textural alignment can be relatively strong. The overall strain history of a rock that now resides in the lower oceanic lithosphere may have been rather complex. Beneath the spreading axis, the rock may have experienced subvertical shearing during upwelling. Upon nearing the surface, upwelling rates decreased, and the lateral motion of the plates became the driving force for further deformation in the sample. Cooling from above would eventually incorporate the rock into a rigid lithosphere, but until that stage is reached, subhorizontal shearing associated with spreading flow would leave its imprint on the mineral texture. This type of complex strain history is not well represented by special cases such as axial compression or progressive simple shear, which have been studied in detail. The orientation of the principal strain evolves continuously along the path that the rock parcel travels. The mineral texture at a given point reflects the response of many, variously oriented grains to the local stresses within the rock and is the result of the accumulated deformation history.

2. Flow Model and Strain Rate Evolution Along Streamlines

[5] Flow in the upper mantle near an oceanic spreading center (Figure 1) is modeled using an iterative two-dimensional finite element method, and the temperature field is computed with an upwind finite difference algorithm [*Turcotte and Phipps Morgan*, 1992; *Jha et al.*, 1994]. The approach is the same as was used in our earlier work [*Blackman et al.*, 1996]. Partial melting, associated with decompression during mantle upwelling, occurs when the liquidus is crossed: $T_m = 1100°C + 3.25(°C/km)z$, where T_m is melting temperature and z is depth in kilometers. A small amount of (matrix) compressibility corresponds to the melt production rate. The small volume of melt is allowed to accumulate and body forces associated with its relative buoyancy are incorporated in the flow solution. The partially melted peridotite matrix is depleted, so its density is lowered; again the associated body forces affect the evolution of the flow field. The plates spreading rate is specified as a velocity boundary condition on the top of the model and the axis of spreading is a mirror plane (plotted at left in Figure 1). A corner flow solution [e.g., *Batchelor*, 1967] is used for the bottom and side boundary conditions, starting at the base of the lithosphere for the latter. Above the lithosphere base, velocity on the side is set to the spreading rate. The base of the lithosphere is defined by the 700°C isotherm, and it is 3 orders of magnitude higher in viscosity than the asthenosphere. For the passive flow models, asthenosphere viscosity is constant at 10^{20} Pa s, and a value of 5×10^{18} Pa s is used for the buoyant flow model discussed in section 5. The full model space extends 250 km from the axis in both x (horizontal) and z (vertical) directions.

[6] Streamlines for slow-spreading (20 mm/yr), passive flow models are used to illustrate the effect of several factors on the development of textural anisotropy. Dozens of streamlines from this and other similar flow fields have been investigated, and we select just a couple to illustrate the results. Our choice of streamlines reflects an emphasis on how continuously evolving strain fields can affect texture development; an aspect that is not easily addressed in laboratory experiments nor always possible to unravel in field specimens. Mineral aggregates that travel along the three chosen streamlines encounter different strain-rate and rotation fields. The changes along streamline 1341 are modest, whereas, in the vicinity of the "corner" in the flow, quite large changes occur along streamline 1322 (Figure 2).

[7] For simulations with the self-consistent polycrystal plasticity approach, an incompressible flow model is required. It turns out that for the slow-spreading, passive flow model this introduces only minor changes to the velocity gradients along a streamline. For incompressible flow we do not allow any melting of the mantle during upwelling. We choose a streamline between 1322, which ends in the shallow lithosphere, and the deeper streamline 1341. The chosen streamline, 1832, provides

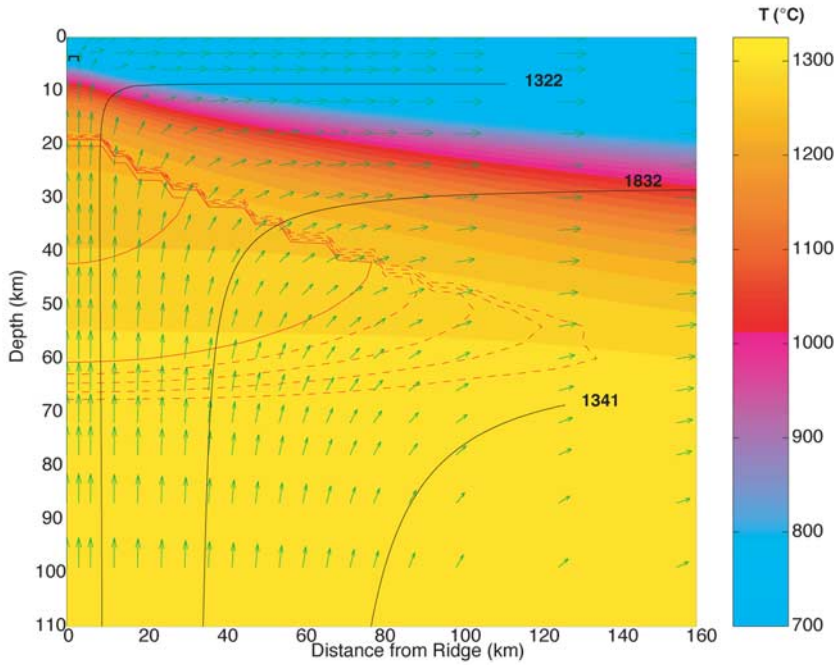

Figure 1. Spreading center flow model with streamlines discussed in the text labeled. Color shows temperature. Green arrows indicate velocity with length scaled to magnitude; lithosphere arrows are 20 mm/yr. Red contours show percent melt present at 1% interval (0.2–0.8 dashed).

significant changes in strain orientation but avoids the very strong gradient region experienced by streamline 1322.

3. Comparison of Polycrystal Plasticity Models

[8] Deformation of a polycrystal is a very complicated heterogeneous process. When an external stress is applied to the polycrystal, it is transmitted to individual grains. Dislocations move on slip systems, dislocations interact and cause ''hardening'' [e.g., *Kocks*, 1976], grains change their shape and orientation, thereby interacting with neighbors and creating local stresses that need to be accommodated. To realistically model these processes is a formidable task and only recently have three-dimensional finite element formulations been developed to capture at least some aspects [e.g., *Mathur and Dawson*, 1989; *Sarma and Dawson*, 1996; *Mika and Dawson*, 1999]. The difficulty is that in real materials local stress equilibrium and local strain continuity are maintained, and this requires local heterogeneity at the microscopic level.

[9] Most polycrystal plasticity simulations have used highly simplistic approximations, for example, that each grain is homogeneous, and yet they have arrived, at least for moderate strains, at useful results. There are two extreme assumptions. *Taylor* [1938] suggested that strain is homogeneous throughout the polycrystal, i.e., all grains deform to the same shape, irrespective of their orientation. For this approach even to be viable, the individual crystals must each be able to accommodate an arbitrary deformation, requiring five independent slip systems. While the Taylor assumption is reasonable for materials comprised of crystals with many slip systems such as cubic metals [*Van Houtte*, 1982], the model is neither applicable to olivine nor to enstatite. *Takeshita et al.* [1990] have used a modification of the Taylor model to simulate deformation of olivine, by relaxing some compatibility requirements. In the Taylor model, high stresses are required to activate slip systems, even in unfavorably oriented grains and the model is therefore known as an upper bound model.

[10] In contrast to the Taylor hypothesis, all crystals in a polycrystal can be required to exhibit identical

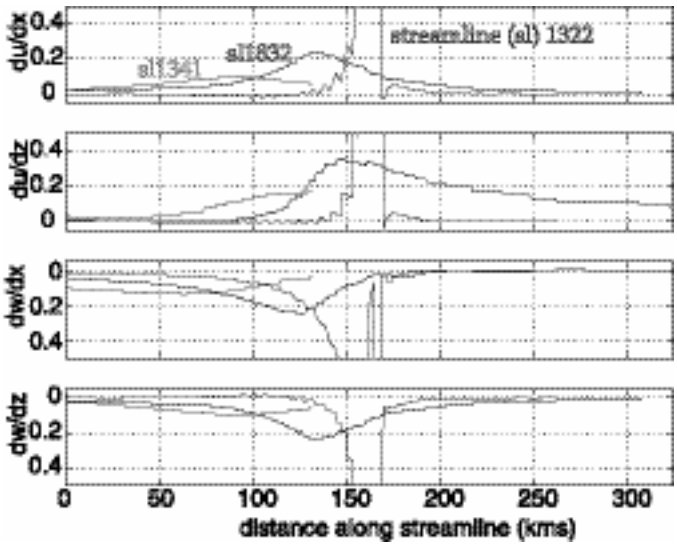

Figure 2. The evolution of strain rate along the streamlines is illustrated by the velocity gradient components of the tensor. Spreading direction corresonds to x and flow component u; vertical direction corresponds to z and flow component w. Distance along the streamlines is calculated for a starting point at 170 km depth in the upwelling zone. Location of the three streamlines is shown in Figure 1. Simple shear conditions occur where only one cross gradient term (du/dz or dw/dx) is nonzero. Within ~60 km of the spreading axis, the highest strain rates occur as each streamline changes direction in the "corner" of the flow field. For streamline 1832, the magnitude of shear in the upwelling region (before the corner) is smaller than it is in the off-axis region. For streamline 1322, peak magnitudes of the strain rate components exceed 1.5–2, where the flow turns the corner near the spreading axis. Subsequently, the aggregate becomes part of the nearly rigid lithosphere and strain rates are quite small.

stress. This is a variant of the original Sachs assumption for rate independent behavior in which the stresses in the crystals throughout an aggregate share a common direction. The equal stress hypothesis is most effective for polycrystals comprised of crystals with fewer than the five independent slip systems. The principal drawback of this model is that deformation is concentrated too highly in a small number of crystals, leading to inaccurate texture predictions. With the Sachs approach only the most favorable slip systems are activated and, therefore, stresses are low. This approach is known as a lower bound model.

[11] Obviously the physically realized case is somewhere between upper and lower bound. Before finite element formulations became available (and those are still by-and-large restricted to cubic metals and require large computing efforts), several other approaches had been developed for modeling the heterogeneous deformation of highly anisotropic polycrystals. For example, *Molinari et al.* [1987] developed the viscoplastic self-consistent (VPSC) formulation in which each grain is regarded as an inclusion embedded in a viscoplastic homogeneous equivalent medium (HEM) whose properties coincide with the average properties of the polycrystal. Originally the VPSC formulation assumed the HEM to be isotropic. A more general formulation, having an anisotropic medium behavior, was introduced by *Lebensohn and Tomé* [1993]. The fully anisotropic VPSC has been fairly successfully applied to the prediction of texture development of various geologic materials (for a review see *Wenk* [1999]).

[12] Use of finite elements to model intragranular heterogeneous deformation on large systems like a mantle convection cell is still out of the question, and we have therefore used the relatively simple and straightforward lower bound (LB) and viscoplastic self-consistent method. Both these methods produce only approximations of the actual physical processes, and results are not perfect predictions. This is particularly true for such anisotropic minerals as olivine and enstatite, and for large strains, where in real situations incompatibilities between grains are large and the topology of the grain

structure changes. In the model, crystal rotations that lead to texture evolution are entirely due to slip. Other processes such as climb and grain boundary sliding may affect textures but are not taken into account. Possible effects of recrystallization will be discussed in section 4.

[13] The VPSC method is in some ways a compromise between stress equilibrium and strain compatibility, though it is much closer to lower bounds than to Taylor. The method has been refined, with adjustable parameters, mainly to improve predictions of mechanical properties [*Molinari and Toth*, 1994; *Molinari*, 1999]. A key feature of the VPSC method is that interaction between an individual grain and the surrounding material is considered. The extent of this interaction can be influenced by the user by either emphasizing stress equilibrium or compatibility. *Tommasi et al.* [2000] have made use of this "tuning" in texture predictions for olivine and observed that resulting differences in textures are minor, particularly when the goal of the modeling is to determine effective seismic properties. With both methods, LB and VPSC, grain reorientations are probably unrealistically rapid [*Chastel et al.*, 1993; *Tomé and Canova*, 1998], and the degree of preferred orientation that develops is probably overestimated, particularly for LB.

[14] The grain/surroundings interaction is strongly nonlinear, since a plastic rheology must be employed for aggregates of minerals with few slip systems. Numerical implementation is achieved by using a locally linearized material response but this restricts the accuracy to deformations in which stress and strain rate changes are not drastic. Also, for large strains (>100%) local heterogeneity in stress and strain, between grains, would need to be taken into account and the finite element procedure developed by Dawson and coworkers [e.g., *Dawson and Beaudoin*, 1998] would be more appropriate for such high strain polycrystal deformation modeling. Neither the LC nor the VPSC model takes complexities of highly deformed grains with large aspect ratios into account and predictions beyond 100% strain are fairly hypothetical.

[15] Olivine grains deform according to the relative ease of slip on several active systems (Table 1), depending on their orientation. Note that in this and all following simulations, we use constant critical shear stresses, even though there are considerable temperature gradients in the system. We do this because only shear stress ratios affect texture evolution. However, simulations will be unrealistic with respect to predictions of flow stress. The strain rate sensitivity of slip is described with a stress exponent $n = 9$ [e.g., *Hanson and Spetzler*, 1994].

Table 1. Slip Systems Used in Texture Calculations

Mineral	Slip-Plane Normal	Slip Direction	Critical Shear Stress[a]
Olivine	(010)	[100]	15 MPa
Olivine	(001)	[100]	16
Olivine	(010)	[001]	40
Olivine	(100)	[001]	35
Enstatite	(100)	[001]	15

[a] Critical shear stresses estimated at 1400°C [from *Bai et al.*, 1991].

[16] The streamline we choose for illustrating the influence of model assumptions on texturing is 1832 (partially shown in Figure 1). The streamline was discretized into 320 steps. At each step we specified the displacement gradient tensor for the flow field at the local position and the time interval corresponding to the increment along streamline between the current and the previous step. Along streamline 1832, strain develops slowly during the upwelling limb of the flow. Within the corner region where flow transitions from vertical to horizontal, strains are high but not as extreme as for flow lines that finish within the shallow lithosphere of the model (Figures 1 and 2). As plate spreading dominates the flow off-axis, the finite strain decreases significantly, since the deformation counteracts the elongation obtained during cornering. A slow rotation of the ellipse continues for a few hundred km off axis (Figure 3). Beyond a distance of about 150 km, essentially simple shear conditions have taken over from the prior, more complex strain field associated with the corner in the flow field. Deeper streamlines turn the corner further from the spreading axis, and this plays a role in the width of the zone for which the strain field is more complex than simple shear. The magnitude of the strain has decreased markedly at a distance of 100 km from the axis. The effect of

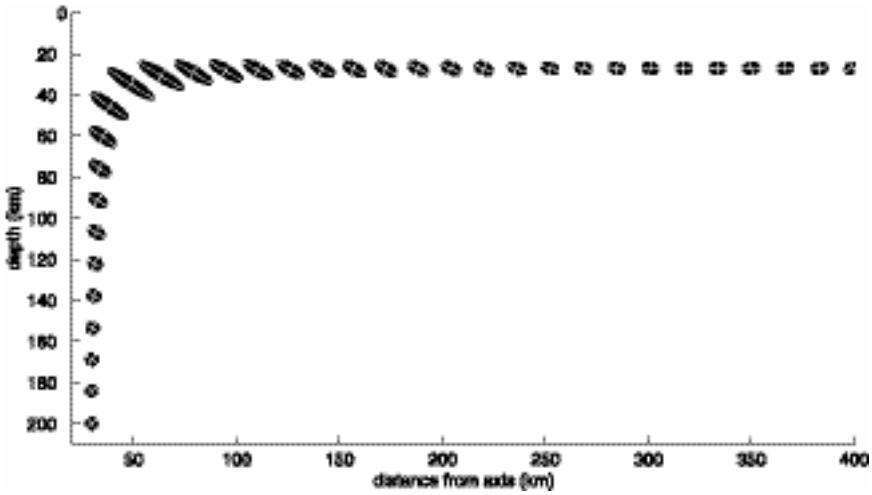

Figure 3. Finite strain evolution along streamline 1832. The minor axis is plotted with a constant length so each symbol shows the relative elongation in the direction of the axes as well as their orientation.

this decrease is that changes in the finite strain ellipse take time to build up, to the point where an orientation that is more typical of what would be expected for simple shearing (if there had been no prior deformation history) is achieved. The major axis of the ellipse parallels the flow line near 350 km distance from the axis of upwelling, but it continues to rotate counterclockwise.

[17] Texture results are illustrated with [100] pole figures (*a* axis of olivine, the single crystal direction with fast *P* wave velocities; Figure 4). For each crystal the full orientation is known at each deformation increment, and this is used for the calculation of elastic properties. In LB and VPSC the preferred orientation that develops in the upwelling portion of the streamline is similar, although the strength of the fabric is stronger in the lower bound model. The greatest degree of olivine *a* axis alignment develops in the corner region. The lower bound calculation produces a bimodal orientation distribution during the spreading-parallel portion of the streamline, although a preference for a subhorizontal concentration of *a* axes is clear (Figure 4). In contrast, the VPSC model shows both some randomization of the strong, corner-related texture and a slower rotation of the preferred orientation direction toward subhorizontal. For the LB and VPSC cases, the *a* axis concentrations rotate 10°–15° beyond horizontal (counterclockwise) toward the finite strain direction near the end of streamline 1832 (Figure 4).

[18] We calculate effective elastic constants for the olivine aggregates by Voigt averaging the single crystal tensors over all the grain orientations. This approach produces effective seismic velocities that agree best with observed average upper mantle values (e.g., PREM), and the difference in the anisotropy produced by Voigt versus Voigt-Reuss-Hill averaging is negligible. Each grain's single-crystal tensor components are projected according to grain orientation with respect to the global frame. Olivine single-crystal constants are taken from *Anderson and Isaak* [1995] and those for enstatite are from *Kumazawa* [1969]. We do not include temperature and pressure derivative terms for the elastic constants, since their effects compete and together they contribute less than a couple percent to the magnitude of the resulting anisotropy, and the change in fast seismic direction is negligible [*Mainprice et al.*, 2000; *Blackman and Kendall*, 2002]. We would need to incorporate the derivative terms if our models included a greater temperature range and/or a greater mantle depth, since the individual C_{ij} derivatives differ by up to 8% (for a 300°C temperature change) and 10% (for a 100 km depth change) [*Estey and Douglas*, 1986].

[19] Figure 5 shows wave surface plots for *P* waves at positions along streamline 1832 that correspond to several of the positions for which pole figures are shown in Figure 4. Each wave surface represents the directional dependence of compressional

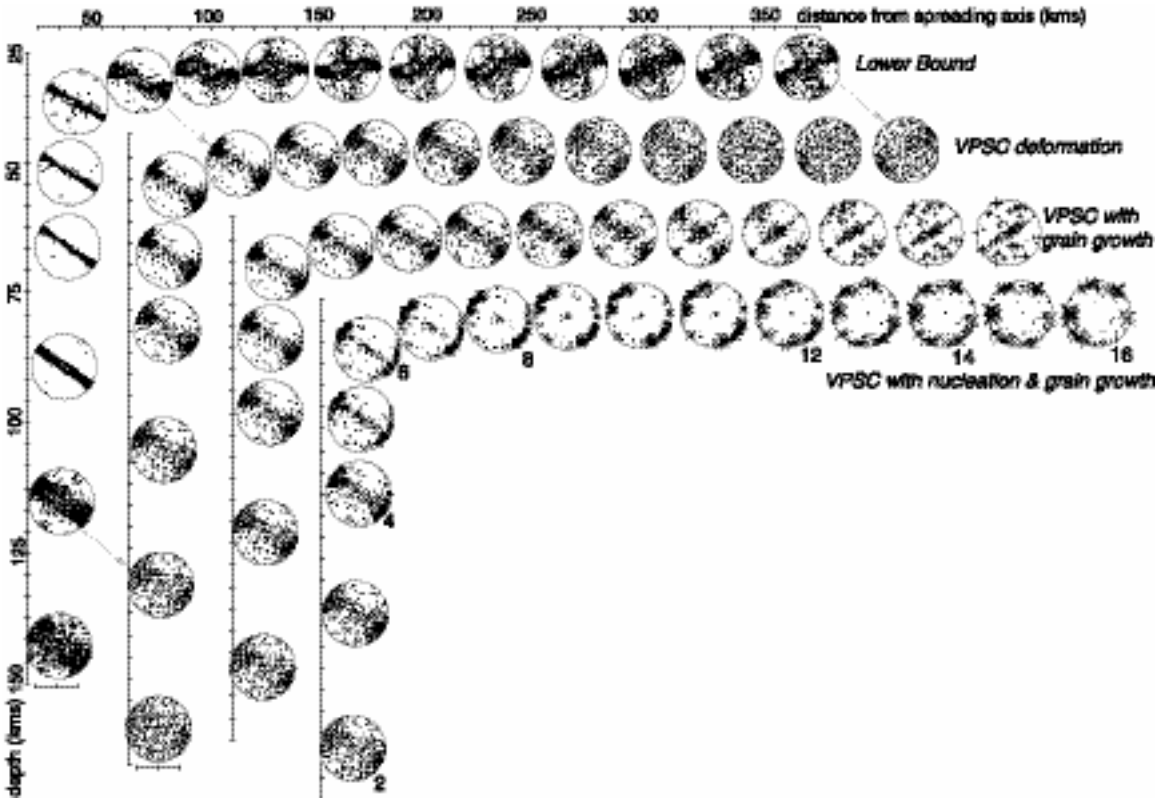

Figure 4. Pole figures show olivine *a* axis, [100], orientation distributions for the four models of texture evolution discussed in sections 3 and 4. Equal area plots are positioned along the streamline to illustrate the evolution of the mineral aggregate. Labels adjacent to the lower bound case indicate the relationship between the streamline (1832 in Figure 1) and the spreading center axis. They apply to all VPSC cases, but the latter have been shifted down and to the right for visibility. Grain growth and nucleation cases (lower 2) include possible effects of recrystallization on texture development. In these plots, pole symbol size is proportional to grain size. The symbol type indicates whether nucleation has occurred (crosses) or not (plusses). Positions corresponding to seismic wave plots shown in Figures 5 and 6 are labeled (2–16).

wave speed for a point source centered at the relevant position. The degree of *P* wave anisotropy $(Vp_{max} - Vp_{min})/Vp_{ave}$ is indicated for each position. Overall patterns for LB and VPSC velocities are similar, but important differences do occur. In concert with the randomization of texture in the VPSC case (Figure 4), the strength of the *P* wave anisotropy along the last third of the streamline is quite a bit lower than is predicted for the LB assumption (2–7% versus ~9.5%). Although for the lower bound case it is difficult to see the significant concentration of *a* axes at the ends of the girdles shown in the pole figures in the corner region (Figure 4), its existence is clearly reflected by the *P* wave velocity surface (Figure 5).

[20] Shear wave splitting associated with the predicted LB and VPSC textures along the streamline is illustrated in Figure 6. Here azimuthal variations in the amount of splitting are shown for a point source in an elastic medium corresponding to each local position. Below each plot the local *S* wave anisotropy is also indicated using the definition 200 $(Vs_{max} - Vs_{min})/(Vs_{max} + Vs_{min})$. The basic pattern of predicted splitting is similar for the two models in the upwelling and corner region, although the amount of splitting in the LB case is greater. Off-axis the patterns differ, although both models predict fairly small amounts of splitting for vertically traveling rays.

4. Texture Development With Recrystallization

[21] At high strains and high temperatures, recrystallization is likely to occur, as the upper mantle

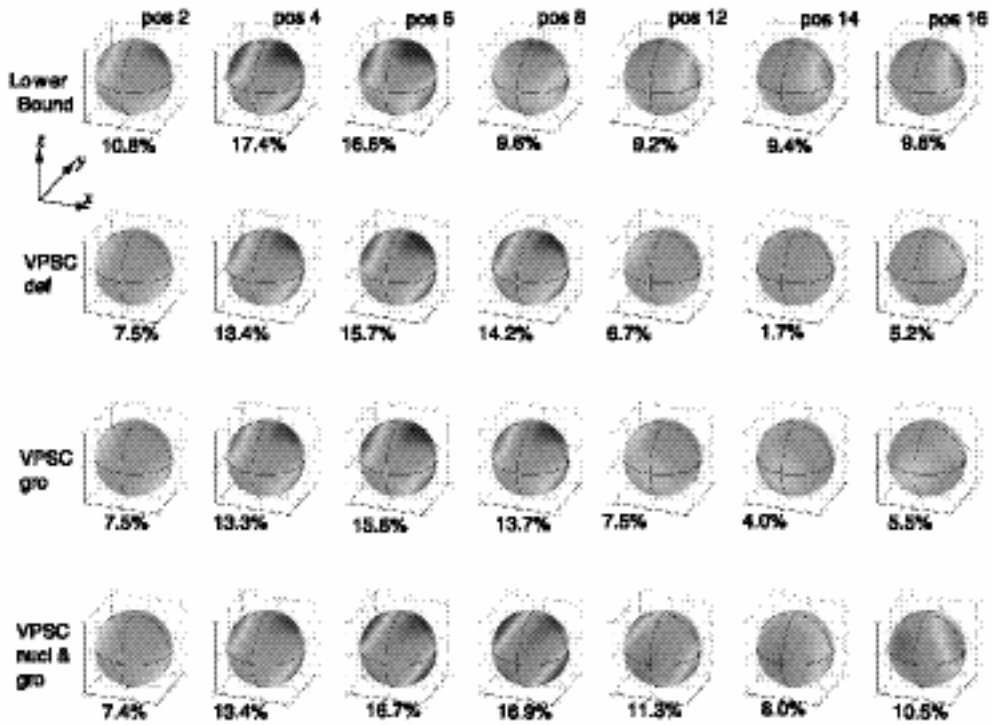

Figure 5. *P* wave velocity surfaces corresponding to olivine orientation distributions for models of texture evolution along streamline 1832. Wave surface plots show azimuthal variation in *P* wave speed for a point source in a medium with effective elastic properties corresponding to each position along the streamline that is shown (locations labeled in Figure 4). Color scale is constant with blue to deep red indicating velocities of 7700–9300 m/s, respectively. Local degree of anisotropy is labeled below each wave surface.

deforms [e.g., *Carter*, 1976; *Karato*, 1988]. The relevant issue here is how this dynamic process may affect the orientation distribution of peridotite minerals. This is a topic that continues to be the focus of both experimental [*Zhang and Karato*, 1995] and modeling investigations [*Wenk and Tomé*, 1999; *Kaminski and Ribe*, 2001]. *Zhang et al.* [2000] report experimental simple-shear results at upper mantle temperatures in which recrystallized grains have orientations similar to their parent grains and are controlled by the geometry of the shearing. However, in some experiments, there are recrystallized grains with different orientations, which reflect the stress direction, as predicted by *Karato* [1986]. *Zhang et al.* [2000] attribute the former recrystallized grain orientations to subgrain rotation, whereas the latter are associated with grain boundary migration processes.

[22] Here we apply a method that balances grain nucleation and grain growth, depending on deformation characteristics [*Wenk et al.*, 1997]. It has previously been applied to olivine [*Wenk and Tomé*, 1999]. We explore how grain growth and/or nucleation may affect the textures that develop along a streamline where flow gradients evolve. This method tracks the degree of deformation in each grain comprising an aggregate, and this deformation is orientation dependent. The grain deformation is related to strain energy, i.e., dislocation densities. Grain growth is determined by comparing a grain's strain energy with that of the aggregate average.

[23] There are two scenarios. In the first one, grains with lower strain energy grow, and those with higher strain energy than the average are consumed

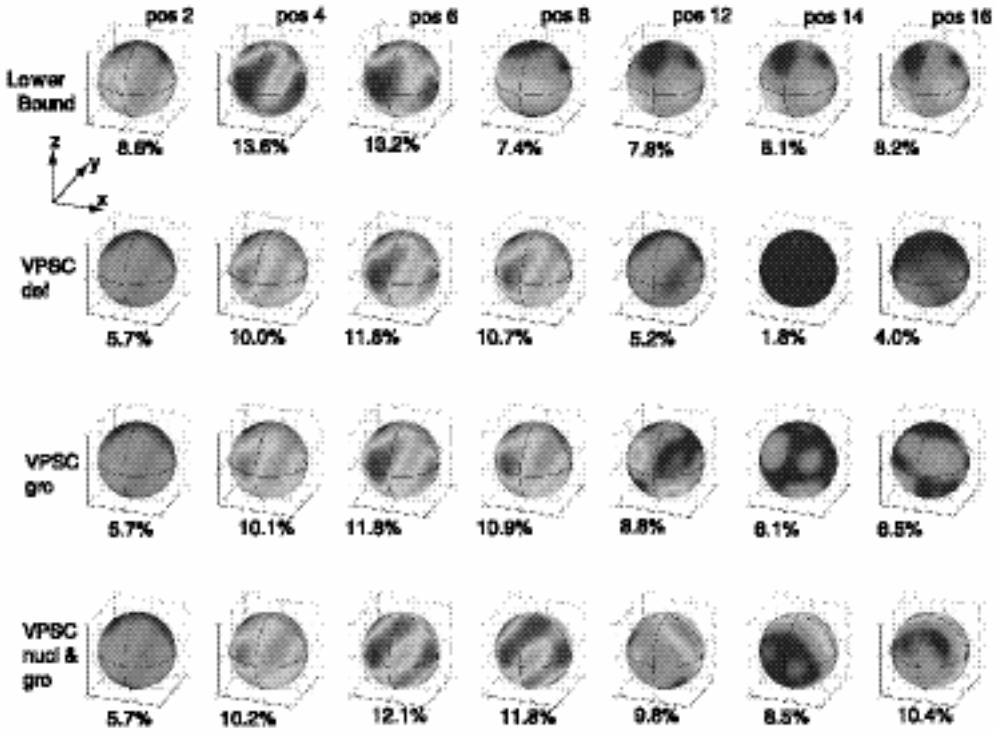

Figure 6. Azimuthal variation in shear wave splitting corresponding to olivine orientation distributions predicted along streamline 1832 for different texture models. Color scale is constant and shows difference in fast and slow shear wave speed from 0–600 m/s, blue to deep red, respectively. Positions shown are the same as in Figure 5, and locations are labeled in Figure 4. Percent *S* wave anisotropy is labeled below each plot.

and in the model assigned a smaller volume after a deformation step. This apportionment is repeated at every step along a streamline. The procedure is intended to produce behavior characteristic of grain boundary migration, and relatively unstrained grains dominate the recrystallization texture. In the second scenario, nucleation of strain-free domains accompanies boundary migration. In this case a highly deformed parent grain divides upon reaching a threshold strain rate and produces an undeformed nucleus. The nucleus (which may be a subgrain or a bulge in a grain boundary) takes on the current orientation of the parent at the time of its formation, but its strain is reset to zero. This has an effect on the subsequent evolution because these strain-free domains can grow much faster. In this case, highly deformed (original) grains dominate the final texture. In the present version of the recrystallization model, no new grains are created. A nucleus forms at the expense of a parent grain. Since some grains are eliminated by shrinkage, the total number of grains is reduced and becomes unrealistically small at large strains. Since the grain number is reduced, the texture strength becomes very large.

[24] Recrystallization conditions in the model are controlled by a few parameters (Table 2). Boundary migration is controlled by a velocity parameter C and a minimum grain volume C_{min} below which a grain vanishes. Nucleation takes place if the strain increment exceeds a threshold value. The threshold B_1 is the percentage of strain increment compared to the maximum strain increment in all grains. For nucleation we also have to specify the initial nucleus size (B_2) and the size when the nucleus becomes a parent (B_3). Recrystallization parameters that we have chosen in this study are similar to those used by *Wenk and Tomé* [1999]. Growth

Table 2. Recrystallization Model Parameters

Parameter	Description	Growth (r3)	Nucleation (r9)
C	growth velocity	25	250
C_{min}	minimum size	10%	10%
B_1	nucleation threshold		85%
B_2	nucleus size		20%
B_3	transfer size		90%

velocities are lower to correspond to the large number of deformation steps. Recrystallization was initiated after 30 steps.

[25] In this paper we investigate the effect of both recrystallization scenarios on seismic velocities. The first set of conditions suppresses nucleation, so recrystallization only takes place by grain boundary migration (this is referred to as "growth" and we show results for a model run labeled "r3"). The second set of conditions favors nucleation but also allows grain growth to occur (it is referred to as "nucleation" and we show results for model run "r9").

[26] For growth-dominated recrystallization, a bimodal distribution develops after the streamline has turned the corner. This is because some stiff, relatively undeformed grains dominate the texture, and more highly deformed grains disappear. Also, the sparse girdle within which the *a* axes had concentrated during upwelling develops a secondary maximum in the direction perpendicular to plate spreading (i.e., ridge parallel). This central pole concentration begins to lose strength and an orientation similar to the deformation-only case begins to take over at the very end of the streamline, as is somewhat more evident in the *P* wave surface plot (Figure 5) than in the pole figure itself (Figure 4).

[27] The nucleation case is the only one for which a streamline-parallel concentration of *a* axes persists beyond ~250 km distance off axis. This is similar to the simulation results of *Wenk and Tomé* [1999] with *a* axes in the shear direction that match the experimental data of *Zhang and Karato* [1995] and *Zhang et al.* [2000].

[28] However, even at the end of the streamline, there are still a number of poles for large grains at other orientations. This produces a range of subspreading-parallel *P* directions for which velocities are significantly greater than at other azimuths and incidence angles (compare the *P* wave surfaces of the lower bound and nucleation cases at position 16 in Figure 5).

[29] *P* wave surface plots (Figure 5) show that the structure predicted to develop along streamline 1832 is similar, at a fundamental level, for all four cases of texturing considered. However, important differences do occur. In concert with the randomization of texture in the VPSC deformation-only case (Figure 4), the strength of the anisotropy along the last third of the streamline is quite a bit lower than is predicted for the LB or nucleation model. *P* wave anisotropies for the latter are just under 5% in the off-axis region (beyond 200 km), whereas the VPSC deformation-only level has dropped to 1–2%. In the growth case, it is the bimodality of the texture off axis that results in a lower effective anisotropy.

[30] The basic pattern of shear wave splitting (Figure 6) associated with the predicted textures is, again, similar between the models for the upwelling and corner region of the flow field but notable differences develop off axis. Whereas the VPSC and growth models would produce very little SKS (near-vertically incident waves) splitting, the nucleation model predicts notable spread between the fast and slow *S*-wave fronts. Almost 500 m separation would occur for every second of travel in rock with fabric like that shown in the pole figure at the end of the streamline. The actual delay between the *S* waves that would be observed at the surface 350 km from the spreading axis would reflect variation in the structure with depth. The lower bound model would produce moderate SKS splitting (200–300 m for every second of travel in such media) beyond about 300 km from the axis than the nucleation model.

5. Texturing of Olivine-Enstatite Aggregates

[31] Several previous polycrystal models of the development of preferred orientation during upper mantle flow considered only olivine [*Chastel et al.*,

1993; *Blackman et al.*, 1996; *Tommasi*, 1998], under the assumption that this dominant and mechanically weaker component in peridotite controlled deformation and texturing. While this is true to first order, enstatite accounts for ~30% of the peridotites in the uppermost oceanic mantle [*Dick et al.*, 1984; *Boudier and Nicolas*, 1995; *Jaraslow et al.*, 1996]. Ultimately, realistic models of the seismic anisotropy need to include the effect of enstatite, its orientation distribution and inherent seismic properties. *Ribe* [1992] included olivine and enstatite in his assessment of the behavior of aggregates under constant plane strain, uniaxial compression, and extension. *Wenk et al.* [1991] and *Chastel et al.* [1993] also included enstatite in texture simulations for axial compression and simple shear but not in more general flow fields, and they did not explore the effect on seismic velocity. Our approach here is to incorporate one aspect of enstatite texturing, reorientation due to plastic deformation by dislocation glide, and to compare how this changes the results from a pure olivine model as texture develops along a streamline with variable ambient strain field. Since our textural results are in line with observations from naturally deformed peridotites, we suggest that this limited approach provides at least a refinement in predictions of anisotropy in the upper mantle.

[32] Like olivine, the fastest direction of *P* wave propagation in enstatite crystals is along the *a* axis, [100] (Figures 7a and 7b). However, shear waves in single crystal enstatite have azimuths of maximum splitting, with respect to the *a* axis, that are quite different from those in olivine crystals. Rather than the maximum splitting directions occurring at 15°–20° from the *c* axis direction, as is the case for olivine (Figure 7c), the enstatite splitting maximum occurs ~25° from the *b* axis (Figure 7d). Splitting in the plane perpendicular to the (010) pole is minimal. In addition to the inherent difference between olivine and enstatite elastic tensors that causes this difference in seismic properties, the two minerals have different deformation mechanisms (Table 1). The result is that the effective elastic constants for deformed polycrystalline aggregates (i.e., peridotite) can produce complexities in shear wave behavior. This is important, since shear wave

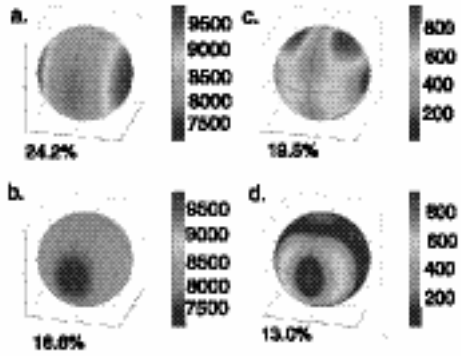

Figure 7. Wave surface plots for single-crystal elastic tensors. The crystal *a* axis [100] is horizontal, the *b* axis [010] points out of the page, and the *c* axis [001] is vertical. The spheres on the left illustrate the anisotropic *P* wave speeds as a function of azimuth. The spheres on the right illustrate the amount of S-wave splitting as a function of azimuth. Percent anisotropy (see text) is labeled below each plot. (a) Olivine P wave speed. (b) Enstatite *P* wave speed. (c) Olivine *S* wave splitting. (d) Enstatite *S* wave splitting.

splitting, and the characterization of fast-*S* polarization direction is a key means of using surface seismic observations to map anisotropy at depth [*Silver*, 1996; *Savage*, 1999].

[33] The lower-bound code was modified so that deformation of an arbitrary ratio of olivine-enstatite grains could be tracked along streamlines of a flow field. We use an approach in which there is no interaction between the two phases and each grain is treated independently. The dominant slip system in enstatite is [001](100) [*Carter*, 1976], and we specified a critical resolved stress of 15 MPa as the threshold for activity of this single system (Table 1). For the results presented here, we used a ratio of 70:30 olivine-enstatite with an initially random orientation distribution of grains at the start of the streamline at the base of the model.

[34] Figure 8 compares the predicted texture after aggregates travel each of two streamlines in a plate-spreading flow model. The olivine-only aggregates experience the same effective (macroscopic) strain as the 70:30 olivine-enstatite aggregates, but the orientation distributions evolve differently due to the presence of enstatite in the mixed sample. The predicted orientation distributions for the 70:30 mix

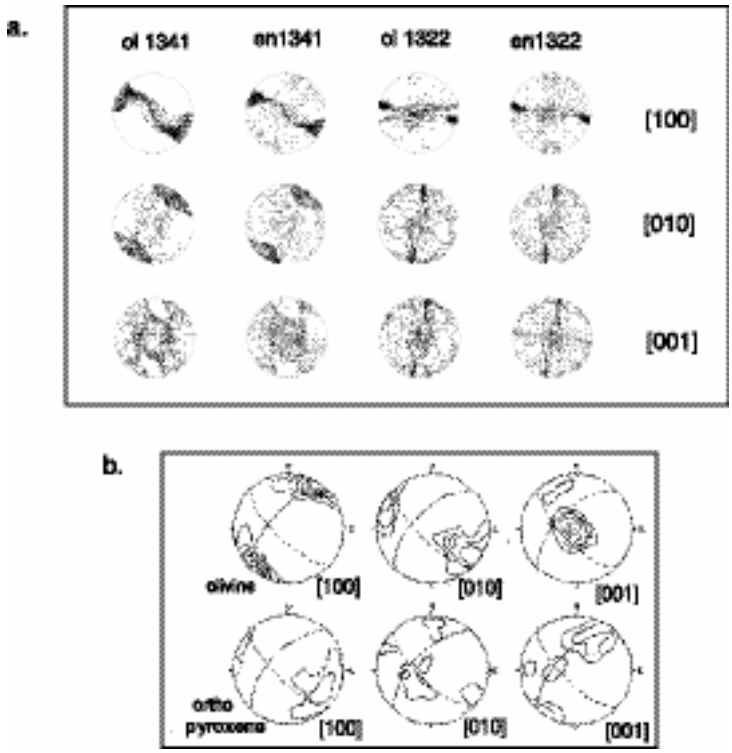

Figure 8. Comparison of texturing for olivine-only aggregates and a mix of 70% olivine with 30% enstatite. (a) Textures calculated with the lower bound method for 1000-grain aggregates are shown for positions at the end of each streamline labeled. Equal area polar nets show black dots for olivine axes, green dots for enstatite axes. Texture at the end of streamline 1341 has strong concentrations of olivine *a* axes (100) inclined 15°–30° clockwise from horizontal. Some poles orient at different azimuths within a plane of this dip as shown by the sparse girdle. The olivine *b* axes (010) concentrate at 90° to the *a* axes and the *c* axes (001) are more dispersed for this strain history. The enstatite grains develop a-axis concentrations at 90° to the plane that contains the olivine (100) poles, enstatite *b* axes are dispersed and the *c* axes form a girdle essentially in the plane of the olivine *a* axes. Textures at the end of streamline 1322 illustrate how a more complex strain history can affect grain orientations. (b) Compilation of olivine and orthopyroxene fabric measured in eight peridotite samples from the Bay of Islands Ophiolite (from *Christensen and Lundquist* [1982]; note that shear plane is rotated 90° relative to Figure 8a) shows that our prediction of the relationship between olivine and enstatite orientation distributions are consistent with naturally occuring fabrics.

are more complex than for the olivine-only case, as expected. Olivine *a* axes in the mixed cases have a tighter concentration and are complemented by enstatite *a* axes that tend to parallel the olivine *b* axes (Figure 8a). The enstatite *c* axes concentrate in the plane that contains the dominant olivine *a* axes concentration. This type of relative olivine and enstatite distribution is similar to what has been documented in peridotite sections of ophiolites, as illustrated in Figure 8b [*Christensen and Lundquist*, 1982; *Boudier and Nicolas*, 1995; *Ben Ismail and Mainprice*, 1998; *Tommasi*, 1998]. All of these ophiolite samples are inferred to represent mantle depths of just a few kilometers, but the same relationship between olivine and orthopyroxene fabric is reported by *Mainprice and Silver* [1993] for kimberlites, which are interpreted to originate at much greater depth in the mantle.

[35] Figure 9 shows wave surface plots for textured aggregates of olivine versus a 70:30 olivine-enstatite mix, corresponding to the results shown in Figure 8. At first glance the color pattern indicates that the velocity patterns are similar. Yet, in detail there are some differences. The degree of *P* wave anisotropy is a few percent lower for the enstatite mix at node position 1341 (Figure 9b shows 11% versus 14% in Figure 9a)), and the maximum shear wave splitting drops 15% between the olivine case and the 70:30 mix. The orientation of the fast *P* direction is essentially the same, and the overall shear wave splitting patterns agree between the

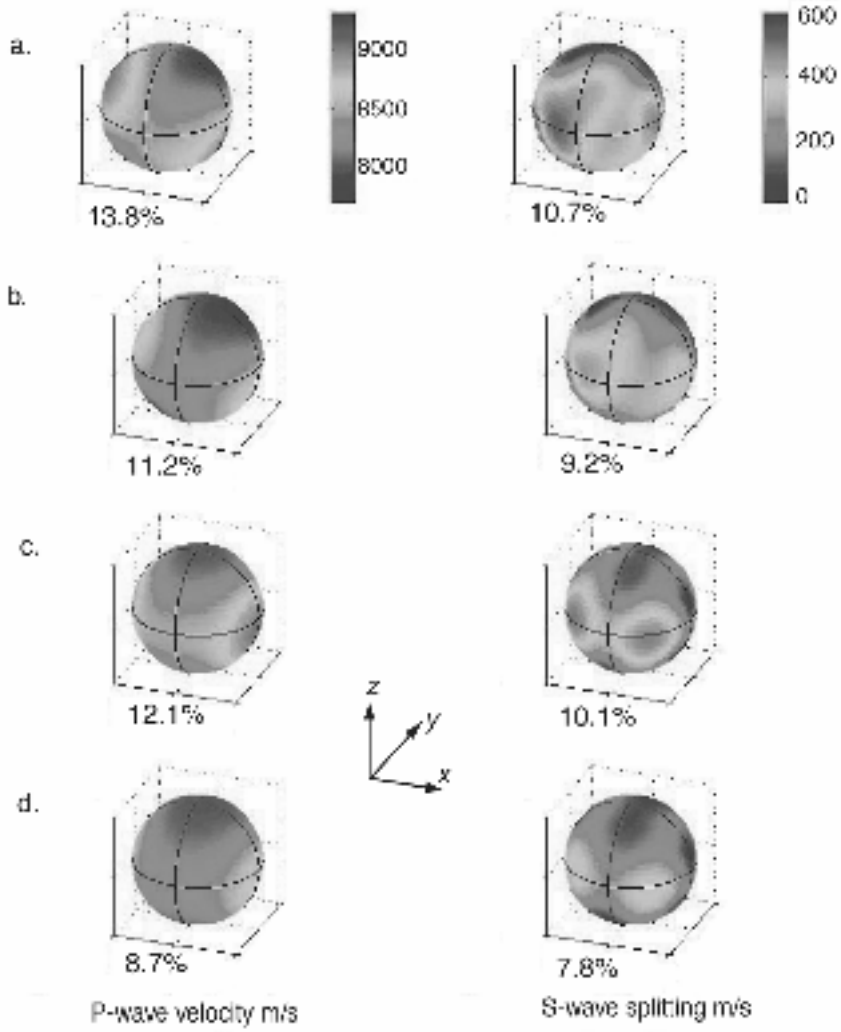

Figure 9. Wave surface plots for a series of rocks with different elastic constants. Azimuthal variation in *P* wave speed (left) and amount of shear wave splitting (right). Local anisotropy for each wave type is labeled below plots. (a) Olivine-only aggregate at the end of streamline 1341 (see Figure 1). (b) 70:30 mix for streamline 1341. (c) Olivine-only aggregate at streamline 1322. (d) 70:30 olivine:enstatite mixed aggregate for streamline 1322.

cases, but the delay between the first and last arriving shear wave is reduced. The amount of reduction depends on azimuth.

[36] These wave surfaces represent seismic properties in the vicinity of a particular position along a streamline. Near node 1322, the aggregate has traveled through the upwelling region, turned the ''corner'' and followed the plate motion for some time. Again, with the inclusion of enstatite, the degree of *P* wave anisotropy decreases a few percent (9% in Figure 9d versus 12% in Figure 9c) and the amount of shear wave splitting is reduced (23% in the direction of maximum splitting).

[37] The polarization direction of near-vertical, fast shear waves is essentially spreading parallel for both nodes 1341 and 1322. Within a typical resolution of several degrees, the angles of fast shear wave polarization are the same for the olivine-only, and the 70:30 olivine-enstatite aggregates for vertical incidence. At node 1322, this agreement between the cases holds for a range of incidence angles (0°–40°) but at node 1341 the fast-*S* polarization angles diverge when incidence angles reach ~20° [see *Blackman and Kendall*, 2002].

[38] The difference in predicted effective aggregate elastic constants for the olivine-only versus the

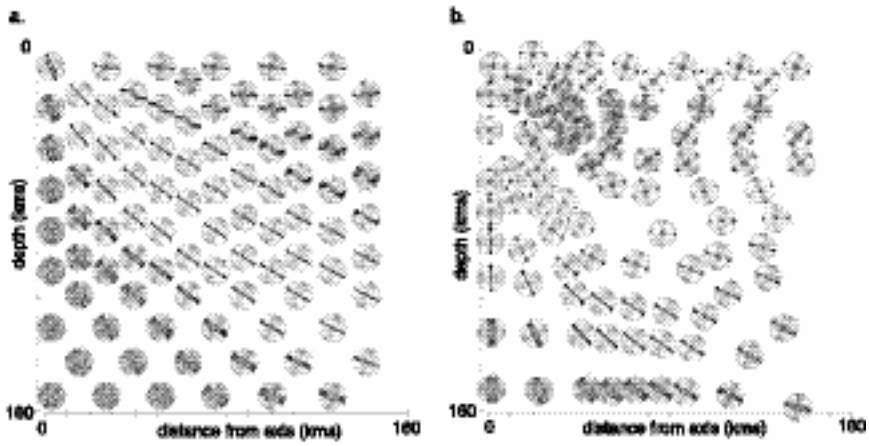

Figure 10. Predicted textures for two different spreading center flow models. (a) Passive flow model-asthenosphere viscosity 10^{20} Pa s. (b) Buoyancy enhanced flow model asthenosphere viscosity 5×10^{18} Pa s. Flow parameters are the same as given by *Blackman et al.* [1996], but texturing begins at 200 km depth and a 70:30 mix of olivine:enstatite grains is used. Pole figures show *a* axis orientation distributions for olivine (black) and enstatite (green).

70:30 olivine-enstatite mix depends on the strain history of the aggregate. For a passive plate-spreading model, the results for streamlines 1341 and 1322 represent the behavior throughout much of the region within a few hundred kilometer of the spreading axis (Figure 10a). This is not the case for a more complicated flow field. When asthenosphere viscosity beneath the spreading center is low, buoyancy forces due to accumulations of melt in the subaxial region can significantly enhance the upwelling rates (Figure 10b). This narrows the width of the upflow, and a tight circulation with high deformation gradients forms above 100 km depth and within 60 km of the axis [*Buck and Su*, 1989; *Scott*, 1992; *Blackman et al.*, 1996]. A bi-polar distribution of crystal *a* axes is produced when streamlines pass through the small circulation region. The enstatite crystals develop *a* axis concentrations perpendicular to the plane of olivine *a* axes concentrations, as before, but now there is also a secondary concentration of olivine *a* axes that coincides with the enstatite *a* axes. Since their single crystal properties have similarities (e.g., the relative magnitude of the diagonal tensor components), the effective anisotropy for these bimodal distributions show only minor differences between the olivine-only and the 70:30 mix cases. As for the passive case, there is not a significant difference in the essentially spreading-parallel polarization angle of the fast shear wave for the two cases.

6. Elastic Tensor Symmetry

[39] The wave surface plots in Figure 9 illustrate how textured aggregates of olivine and enstatite have effective elastic constants that differ significantly from single-crystal tensors. It is the symmetry of the orientation distribution that determines the symmetry of the aggregate and averaging over the grains results in a degree of anisotropy that is lower than the single crystal value [*Kocks et al.*, 1998]. In general, the symmetry of the elastic tensor can be as low as triclinic so that characterizing the seismic anisotropy requires 21 independent constants. Unfortunately, this is far more parameters than can be resolved by seismic observations. Consequently, surface seismic experiments and the interpretations of *P* wave travel times, shear wave splitting and polarization directions, and surface wave data are almost always approached using a simplified symmetry model for the inferred anisotropy [*Hess*, 1962; *Backus*, 1965; *Nishimura and Forsyth*, 1989; *Silver and Chan*, 1991; *Savage*, 1999]. The most common approach is to assume hexagonal symmetry. The ''fast axis'' in this case refers both to the direction of maximum *P* wave propagation speed and the

direction in which the fastest of the two shear waves is polarized.

[40] Previous studies show how depth variations in the azimuth of a horizontal fast axis can affect shear wave splitting and surface wave anisotropy signals [*Shimamura*, 1984; *Nishimura and Forsyth*, 1989; *Silver and Savage*, 1994; *Rümpker et al.*, 1999; *Saltzer et al.*, 2000; *Schulte-Pelkum*, 2001]. *Sileny and Plomerova* [1996] show that the assumption of a horizontal fast axis for hexagonal symmetry can introduce significant bias if, in fact, the fast axis dips more than a few degrees relative to the Earth's surface. Here we compare how estimates of the degree of anisotropy would vary as a function of the symmetry assumed for effective elastic constants.

[41] Effective elastic constants for the textured aggregates in our spreading center flow model are computed at positions about 6 km apart. These elastic tensors have 21 independent values and constitute the "full model" symmetry case in the following discussion. Since the flow is two-dimensional (plane strain), the symmetry of the deformation is very close to monoclinic (13 elastic constants), but there are slight deviations due to the asymmetric distribution of initial random orientations and statistics. This results in eight constants that are very small but not strictly zero.

[42] The fast *P* wave direction computed for the full symmetry elastic tensor at a given position is used to anchor the estimates for the higher symmetry cases. Rotating into the frame of the fast *P* axis, a linear least-squares regression is used to determine the five elastic constants for a hexagonal model that best fits the local full symmetry model. For the orthorhombic estimate, the four nonorthorhombic constants in the monoclinic model are simply set to zero in the rotated reference frame.

[43] The orthorhombic model satisfactorily represents the full *P* wave anisotropy and the shear wave behavior that would occur within local regions throughout the model space (Figure 11). The hexagonal model captures neither the full range of *P* wave anisotropy nor the character of shear behavior in regions of high flow gradients. *P* wave anisotropy values drop ~5% from the full model to the hexagonal best-fit case in the most intensely deforming regions. Similarly, the full symmetry models show considerable variation with direction of both fast and slow shear wave speeds, but the hexagonal cannot.

[44] The plots in Figure 11 provide useful insight into what regions of the model are well represented by hexagonal symmetry assumptions and where such simplifications are misleading. The basic pattern of anisotropic structure is similar for all three symmetry assumptions. The thickening of the (rigid) lithosphere in proportion to the square root of plate age dominates the pattern. The highest degrees of anisotropy accumulate near the base of the plate and their depth extent increases with distance off axis. The distribution of regions in which anisotropy is greatest in the full symmetry model are not well matched in the hexagonal model for either *P* or *S* waves. The poorly matched region is fairly thin (i.e., short travel times through this section for near-vertical incidence; Figure 11, left panels) for *P* waves, but for *S* waves the region is quite a bit larger (Figure 11, center and right panels).

[45] Surface seismic recordings integrate over the variable anisotropic structure, so it is important to illustrate how body wave travel times and shear wave splitting are affected by the simplified symmetry assumptions. The wave propagation modeling simulates an array of ocean bottom seismometers crossing the plate boundary with an aperture of a few hundred kilometers and instrument spacings on the order of several kilometers. The seismic waves respond only to the anisotropic structure corresponding to effective elastic constants for the textured aggregates. In order to highlight the textural anisotropic signals, we have ignored possible heterogeneity and anisotropic contributions of melt generated during mantle upwelling [*Forsyth*, 1992; *Faul et al.*, 1994; *Blackman and Kendall*, 1997].

[46] Asymptotic ray theory is used to model wave propagation in both the passive and buoyancy-enhanced spreading flow models. The details of the ray tracing are described by *Blackman et al.* [1996]. Ray theory is a high-frequency approximation that neglects effects like mode coupling between the fast and slow shear-waves. There is no general rule to describe the limitations of

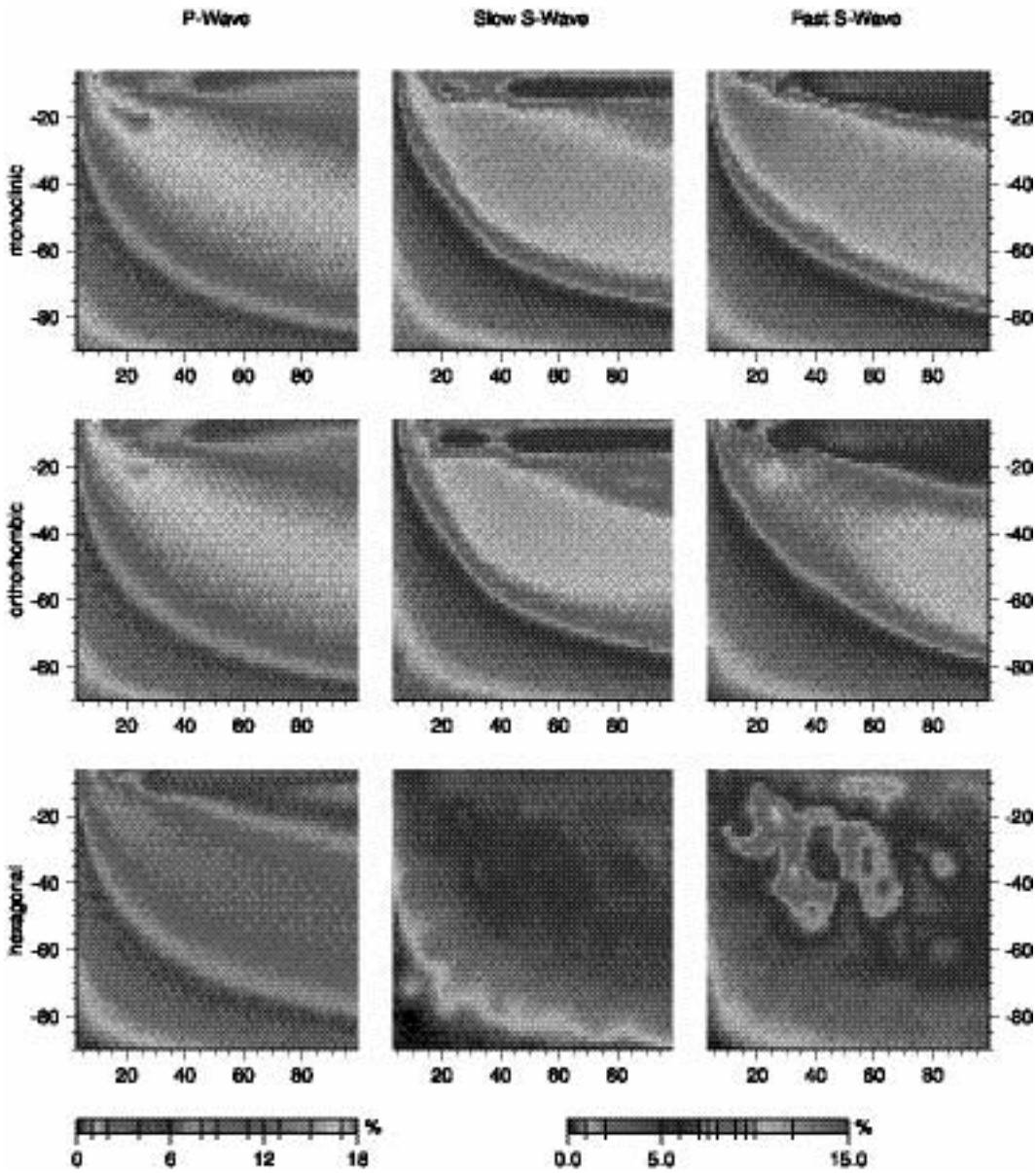

Figure 11. Comparison of anisotropic structure for different assumed elastic symmetries-passive flow model (Figures 1 and 10a). For *P* waves (left column), the local anisotropy in the model plane is shown by color shades for each symmetry case. For *S* waves there is also a dependence of velocity on incidence angle. This can be defined similar to the *P* wave anisotropy for each of the shear waves. The middle and right columns show the local variation in the slow and fast shear wave speed, respectively, for each symmetry estimate.

modeling wave propagation using ray theory since the extent of any limitations depends strongly on the distribution of elastic properties of a given model. To determine whether ray theory provides a reasonable approach for a particular model, two scales in both space and time need to be considered. These are the (spatial) width of the seismic wave pulse, the length scale over which the instantaneous wavefront curvature changes, and the timescales of the pulse width and of any significant features in the ray travel-time curve. There is little structural complexity in our models and the wavelength of teleseismic phases in the uppermost mantle is of the same scale as our grid spacing. Thus ray theory should do a reasonable job of predicting realistic waveforms. A perturbation approach like that of *Rümpker et al.*

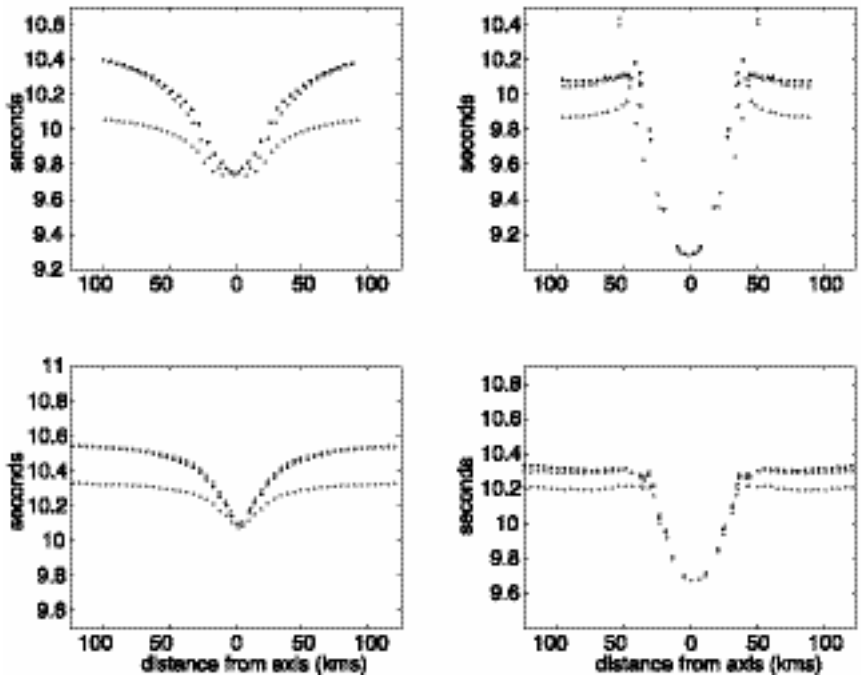

Figure 12. Comparison of near-vertical compressional wave travel time delays for the different elastic symmetry approximations: full symmetry model (black); orthorhombic approximation (red); hexagonal approximation (green). Passive plate spreading flow model (left), buoyancy enhanced spreading flow model (right), olivine-only aggregate (top), and mixed 70:30 olivine:enstatite aggregate (lower).

[1999] could not be used to investigate coupling effects on apparent shear wave splitting as there are regions of the model where the anisotropy is strong. Full waveform techniques [e.g., *Hung and Forsyth*, 1998; *Komatitsch et al.*, 2000] could be employed to accurately model the waveforms, but these methods are quite computationally challenging. Ray theory has an advantage in that the analysis is localized to a given wave type, thus illuminating model sensitivity more easily.

[47] A comparison of body wave travel times for rays that travel vertically through a series of models is shown in Figure 12. The relative travel times predicted for the orthorhombic symmetry approximation match the full symmetry predictions quite well for both the passive and buoyancy-enhanced models. This holds for both PKP and SKS waves. Relative delays that are predicted for the hexagonal approximation are 0.1–0.4 s less than those predicted for the full symmetry case. This is a significant portion of the total predicted anomaly, and it indicates that a travel time inversion that assumes hexagonal symmetry will overestimate the magnitude of the actual anisotropy. This would occur since greater degrees of anisotropy would be required, during the hexagonal forward calculation step, to achieve a given travel time anomaly magnitude. However, the nature of the relative travel time anomalies is similar for all of the symmetry cases so qualitative interpretations would not suffer from a simpler elastic symmetry assumption for this type of model.

[48] Wave propagation through olivine-enstatite models are also shown in Figure 12. The predicted travel times clearly show that the full symmetry and orthorhombic models agree to within the resolution of ocean-bottom recordings. The hexagonal models underestimate the variations in travel-times by 0.2–0.4 s, the largest differences occurring for the passive models. The results for vertically travelling *S* wave in the passive model with a olivine-enstatite composition are shown in Figure 13. Again the full symmetry and orthorhombic models show good agreement, while the hexagonal model significantly overestimates the amount of splitting in the region within 30 km of the axis (0.8 versus 0.4 s of splitting).

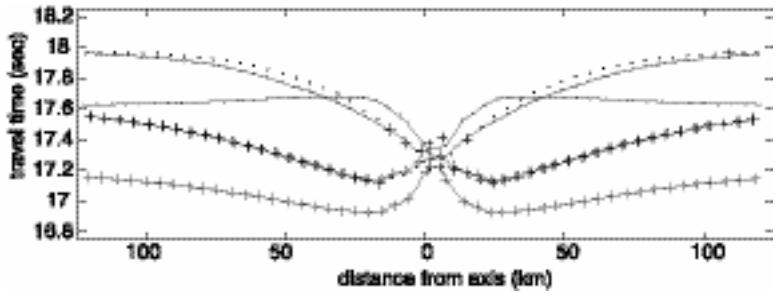

Figure 13. Comparison of SKS splitting predicted for a passive plate spreading flow model. Full symmetry (black), orthorhombic approximation (red), hexagonal approximation (green). Different symbols denote the two shear waves for each case.

[49] The predicted polarization direction of the fast shear wave varies somewhat for the different symmetry models although the variation is near the level of uncertainty with which seafloor data analyses can be done (±10° [e.g., *Wolfe and Solomon*, 1998; *Forsyth et al.*, 1998]). The full symmetry case is characterized by a dominantly spreading parallel fast *S* wave polarization direction for near-vertical incidence. Only a narrow region beneath the spreading axis shows ridge-parallel polarization directions and most of this region has low splitting magnitudes for SKS. Within the lithosphere of this passive spreading flow model, the polarization directions predicted for orthorhombic and hexagonal symmetry approximations agree with the full symmetry case. However, throughout the asthenosphere, these simpler symmetry models predict polarization angles that are rotated 10°–20° (toward ridge-parallel) from the spreading direction. For other incidence angles, this difference in symmetry models persists (and even for the full symmetry model, there are significant changes in predicted fast polarization angle for incidence greater than ∼15° [see *Blackman and Kendall*, 2002]).

[50] Texturing begins at an arbitrary 100 km depth for all models shown in Figure 12. Travel time anomalies for a 200 km texturing onset depth are not detectably different (<0.1 s) for the passive flow model. The olivine-only models produce larger travel time variations than those with the olivine-enstatite mixture. This is due to a combination of lower degrees of anisotropy for the 70:30 cases (section 5) and the juxtaposition of upwelling-induced textures and plate-spreading-induced textures with fast/slow directions that differ by several tens of degrees.

7. Discussion and Conclusions

[51] The results presented here illustrate how predictions of seismic anisotropy due to lattice preferred orientation of upper mantle minerals might vary, depending on model assumptions. Although the examples shown are for mantle flow near an oceanic spreading center, the magnitudes of the deformation gradients in our model are similar to what might be expected to occur in the upper mantle near either a transform or a convergent plate boundary as well. It is the gradients in flow velocity, and their variation along a streamline, that control the evolution of mineral texture as a volume of rock deforms.

[52] The two polycrystal plasticity models compared, lower bounds and viscoplastic self-consistent, predict similar texture patterns but the texture strength of the LB model is significantly larger. In some parts of the LB model the predicted fabric strengths are higher than the average strength found in natural deformed olivine rocks, although the levels of predicted anisotropy fall well within the range of measurements on ophiolite samples [e.g., *Ben Ismaïl and Mainprice*, 1998].

[53] Recrystallization can produce a range of modifications to textures formed by dislocation glide, depending on the mechanism that is operative. The modeling results presented in section 4 present two extreme cases. In the first, grain growth dominates,

and in the second, nucleation plays a strong role. The fabric results for both recrystallization cases differ, in turn, from those that develop when only plastic deformation is simulated. In view of the limits of our current understanding of olivine deformation at upper mantle conditions, it is not possible to determine which model best represents the real case, which also may vary according to location. However, it is likely that the three models represent extreme situations and that the real case is somewhere in between. Recent experimental work suggests that it may be more common for olivine *a* axes to rotate into the shear plane in high strain conditions [*Zhang et al.*, 2000]. This would tend to favor our nucleation model over the others. However, uncertainties in both experimental and field conclusions must be kept in mind at this stage. The experimental results of *Zhang et al.* [2000] suggest that, in at least some cases, grain boundary processes and the orientation of new grains may be strongly affected by local stresses, rather than the shear plane controlling alignment. *Zhang et al.* [2000] also mention the potential importance of grain size distribution, and perhaps the role of water, in their samples. As is usual for any experiments, there is considerable extrapolation of laboratory conditions to mantle conditions that adds uncertainty, most significantly in terms of strain rate.

[54] Field and sample work by A. Nicolas and coworkers (see *Nicolas* [1989], *Boudier and Nicolas* [1995], and the compilation by *Ben Ismaïl and Mainprice* [1998]) indicate that shear-induced fabrics (as opposed to stress-controlled) are most common in the upper mantle sections of ophiolites. In such field analyses, uncertainty arises from ambiguities in determining the paleostrain field from microstructures and textures. In mantle rocks that are juxtaposed with the crust, it is often difficult to determine an original foliation plane and shear plane. Commonly the local orientation of the crust/mantle interface is inferred to represent the shear plane attitude. This is a reasonable approach, but the uncertainty due to measurement error and the possibility that the interface deviates locally from the regional (paleo) shear plane, is probably as large as the 10°–20° difference between the streamline-parallel and finite-strain-parallel directions in the off axis region of our plate spreading model. In this paper we have only briefly touched on texturing in the shallowest (lithospheric) mantle, but it is in this region that ophiolite observations can provide the most constraints. Indications of a reversal in shear sense at shallow depth and a consistent monotonic decrease in shear strain with depth, for example [e.g. *Ceuleneer and Rabinowicz*, 1992], support interpretations of a detailed flow pattern in Oman and the Bay of Islands. In order to numerically investigate this and other possible hypotheses, significantly more detailed tests of the sensitivity of our texture predictions to assumed strain increment along a streamline, and of the ability of either lower bound or VPSC method to capture the essence of polycrystalline behavior at high strain will be required. Two aspects are key to such future studies: the tight curvature of streamlines that end in the shallowest mantle results in very high strains, and our numerical methods become tenuous; these uncertain textures become frozen within the lithosphere very soon after transiting the shallow corner region.

[55] We find that estimates of effective elastic constants obtained when plastic deformation of enstatite is included directly in simulations of texturing provide seismic properties that are in line with values inferred from seafloor and continental measurements (several percent, averaged over regions tens to 100 km in extent). The orientation distributions predicted for a 70:30 mix of olivine-enstatite crystals are similar to that observed in mantle samples from ophiolites. We do not expect that our predictions represent all the processes that will occur as a given volume of peridotite deforms in the upper mantle. Further constraints are needed in the form of additional documentation of the fabrics of both olivine and pyroxene crystals in naturally deformed rocks and the mechanisms that are active, especially consideration of the prismatic shape of enstatite crystals. *Jaraslow et al.* [1996] begin to address this issue for abyssal peridotites; however, their emphasis is mainly on mylonite samples that reflect lithospheric deformation, particularly the formation of shear zones. Laboratory experiments that document the extent of interplay between

olivine and pyroxene crystals during deformation, as well as any crystal shape effects on the resulting texture, will be important. For field constraints, the following questions arise: Are there changes in the olivine versus pyroxene fabrics between samples from inferred upwelling regions (the Oman diapirs studied by the Montpellier group [*Nicolas*, 1989; *Ceuleneer and Rabinowicz*, 1992]) versus inferred off-axis samples? Can one distinguish between olivine-pyroxene fabric measurements at fast-spreading systems (e.g., Oman) versus slow-spreading systems (e.g., Bay of Islands, Cyprus)?

[56] We have focused on textures that develop during mantle flow in the vicinity of a spreading plate boundary. One important difference between mantle flow near-spreading centers and that near subduction or transform boundaries is that the peridotite mantle melts partially due to decompression of the rock as it rises beneath the axis. The resulting basaltic melt eventually segregates and rises to become oceanic crust. *Mainprice* [1997] has discussed the influence that the melt beneath a spreading center could have in attenuating seismic energy beneath the axis and this clearly needs to be considered in a complete model. There are many unresolved questions about the distribution of the melt, as it is produced, and the nature of its route through the mantle, as it proceeds toward the surface [*Kohlstedt*, 1992; *Faul et al.*, 1994; *Kelemen et al.*, 1997]. In view of this uncertainty, we have chosen an end member approach in our modeling. Although we include the generation of melt in the flow calculation, we do not account for any change in deformation processes that might be associated with the presence of melt. In effect we are assuming that the mantle matrix remains connected and that processes along grain boundaries are not altered to the extent that diffusion creep takes over from dislocation glide. As experimental and field observations continue to provide new data, we can incorporate the possible effect of melt in the texture calculations, if it becomes possible to describe the relative importance of different mechanisms quantitatively. At this time we prefer not to assign ad hoc properties to the melting region ($\sim$70–20 km depth and within 40–60 km of the spreading axis).

[57] Of course anisotropic effects associated with preferential alignment of the melt could contribute to the overall seismic structure beneath the axis. We cannot rule out this possibility, but we note that results to date are quite model dependent. The models considered by *Blackman and Kendall* [1997], with a range of possible melt distribution styles and melt contents up to a several percent, resulted in textural anisotropy that overwhelmed the anisotropy corresponding to alignment of melt. *Mainprice* [1997] calculated a somewhat greater effect of ellipsoidal melt inclusions on the overall anisotropy at similar melt contents but for a single assumed background textural anisotropy.

[58] When the degree of anisotropy is low, simple approximations to the full symmetry class of the effective elastic tensor can represent the structure fairly well, as has been shown in different ways previously. However, when the strength of the anisotropy exceeds 5–10%, there is notable difference in the estimated seismic properties and travel time anomalies for low symmetry versus for a hexagonal approximation of the symmetry. Use of an orthorhombic approximation of the elastic tensor does provide a good match to the triclinic or monoclinic cases, even in regions of rather complex strain history. We are not suggesting that travel-time inversions should attempt to solve for nine elastic constants. Rather, our results indicate that, while qualitative inferences from anisotropic inversions with hexagonal symmetry are likely to be useful, quantitative conclusions could be biased. One way to limit the bias would be to perform a few forward models of wave propagation using orthorhombic elastic symmetry. A reference forward model could assume a distribution and degree of anisotropy like that determined in the hexagonal symmetry inversion but with orthogonal elastic constants. Next, a few perturbation cases, where strength/distribution of anisotropy are pushed away from the starting model, could be run. This would illustrate how far the structure, with more realistic elastic properties, could vary from the inversion solution before the match to the seismic data becomes unacceptable.

[59] There is a fair amount of overlap in the *P* wave anisotropy patterns predicted for the different texture models investigated. This is in agreement with previous work employing simple deformation paths [*Tommasi et al.*, 2000], and it gives us a measure of confidence for pursuing how different flow fields affect the seismic structure [*Blackman and Kendall*, 2002]. Although we can expect that the least computationally demanding lower bound method may miss some details and it probably responds too rapidly to changes in the strain field, the general pattern of anisotropy determined will not be way out of line with what the other methods would predict. To understand how the shear wave structure that is predicted for the different textural models might affect observed splitting and surface wave propagation, it is necessary to model more than a single streamline. We begin such investigation using the lower bound case in a companion paper [*Blackman and Kendall*, 2002], but additional exploration of results, when recrystallization is allowed to play a role, may be worthwhile in the future.

[60] Finally, we note that some care is required when applying notions developed based on progressive simple shear results in an ad hoc manner to flow fields that are actually more complex. *Ribe* [1989] pointed this out before, and our new results emphasize the point. The major change in strain field such as will occur within a few hundred kilometers of all plate boundaries introduces complex behavior as polycrystalline peridotite responds and accommodates radically different forces. In our spreading center models, after aggregates have transited the upwelling region and turned the corner to follow plate motion, there is the strongest effect of recrystallization on subsequent texturing. The fact that strong preexisting texture must be altered plays an important role in the evolution of orientation distributions; it is not the same as starting at the ridge axis with randomly oriented grains.

Acknowledgments

[61] We thank Paul Dawson and Donald Boyce for their generosity in providing the lower bound code and taking the time to help us get started working with it. Carlos Tomé also contributed via helpful interaction and discussions. Reviews by Greg Hirth, Neil Ribe, David Mainprice, and Peter Kelemen were helpful for clarifying our results and better emphasizing their context. We appreciate these colleagues' input and their patience in wading through both this and the companion manuscript. Blackman was supported by NSF grant OCE98-12560 for this study and Wenk was supported by IGPP-LANL and NSF EAR 99-02866.

References

Anderson, O. L., and D. B. Isaak, Elastic constants of mantle minerals at high temperature, in *Global Earth Physics: A Handbook of Physical Constants*, *AGU Reference Shelf Ser.*, vol. 1, edited by T. J. Ahrens, AGU, Washington, D. C., 1995.

Backus, G. E., Possible forms of seismic anisotropy of the uppermost mantle under oceans, *J. Geophys. Res.*, *67*, 4427–4440, 1965.

Bai, Q., S. J. Mackwell, and D. L. Kohlstedt, High temperature creep of olivine single crystals, 1, Mechanical results for buffered samples, *J. Geophys. Res.*, *96*, 2441–2463, 1991.

Batchelor, G. K., *An Introduction to Fluid Mechanics*, 615 pp., Cambridge Univ. Press, New York, 1967.

Ben Ismaïl, W., and D. Mainprice, An olivine fabric database: An overview of upper mantle fabrics and seismic anisotropy, *Tectonophys.*, *296*, 145–157, 1998.

Blackman, D. K., and J.-M. Kendall, Sensitivity of teleseismic body waves to mineral texture and melt in the mantle beneath a mid-ocean ridge, *Philos. Trans. R. Soc. London Ser. A.*, *355*, 217–231, 1997.

Blackman, D. K., and J.-M. Kendall, Seismic anisotropy in the upper mantle, 2, Predictions for current plate boundary flow models, *Geochem. Geophys. Geosyst.*, *3*(9), 10.1029/2001GC000247, 2002.

Blackman, D. K., J.-M. Kendall, P. R. Dawson, H.-R. Wenk, D. Boyce, and J. Phipps Morgan, Teleseismic imaging of subaxial flow at mid-ocean ridges: Travel-time effects of anisotropic mineral texture in the mantle, *Geophys. J. Int.*, *127*, 415–426, 1996.

Boudier, F., and A. Nicolas, Nature of the Moho transition zone in the Oman ophiolite, *J. Petrol.*, *36*, 777–796, 1995.

Buck, W. R., and W. Su, Focused mantle upwelling below mid-ocean ridges due to feedback between viscosity and melting, *Geophys. Res. Lett.*, *16*, 641–644, 1989.

Carter, N. L., Steady state flow of rock, *Rev. Geophys.*, *14*, 301–360, 1976.

Ceuleneer, G., and M. Rabinowicz, Mantle flow and melt migration beneath oceanic ridges: models derived from observations in ophiolites, in *Mantle Flow and Melt Generation at Mid-Ocean Ridges*, *Geophys. Monogr. Ser.*, vol. 71, edited by J. Phipps Morgan, D. K. Blackman, and J. M. Sinton, pp. 123–154, AGU, Washington, D. C., 1992.

Chastel, T. B., P. R. Dawson, H.-R. Wenk, and K. Bennett, Anisotropic convection with implications for the upper mantle, *J. Geophys. Res.*, *98*, 17,575–17,771, 1993.

Christensen, N. I., and S. M. Lundquist, Pyroxene orientation in the upper mantle, *Geol. Soc. Am. Bull.*, *93*, 279–288, 1982.

Dawson, P. R., and A. J. Beaudoin, Finite-element simulation

of metal forming, in *Texture and Anisotropy*, edited by U. Kocks, C. Tomé, H.-R. Wenk, pp. 532–559, Cambridge Univ. Press, New York, 1998.

Dawson, P. R., and H.-R. Wenk, Texturing of the upper mantle during convection, *Philos. Mag. A*, *80*, 573–598, 2000.

Dick, H. J. B., R. L. Fisher, and W. B. Bryan, Mineralogic variability of the uppermost mantle along mid-ocean ridges, *Earth Planet. Sci. Lett.*, *69*, 88–106, 1984.

Estey, L. H., and B. J. Douglas, Upper mantle anisotropy: A preliminary model, *J. Geophys. Res.*, *91*, 11,393–11,406, 1986.

Faul, U. H., D. R. Toomey, and H. S. Waff, Intergranular basaltic melt is distributed in thin, elongated inclusions, *Geophys. Res. Lett.*, *21*, 29–32, 1994.

Forsyth, D. W., The early structural evolution and anisotropy of the oceanic upper mantle, *Geophys. J. R. Astron. Soc.*, *43*, 103–162, 1975.

Forsyth, D. W., Geophysical constraints on mantle flow and melt generation beneath mid-ocean ridges, in *Mantle Flow and Melt Generation at Mid-Ocean Ridges*, *Geophys. Monogr. Ser.*, vol. 71, edited by J. Phipps Morgan, D. K. Blackman, and J. M. Sinton, pp. 1–66, AGU, Washington, D. C., 1992.

Forsyth, D. W., S. C. Webb, L. M. Dorman, and Y. Shen, Phase velocities of Rayleigh waves in the MELT experiment on the East Pacific Rise, *Science*, *280*, 1235–1238, 1998.

Hanson, D. R., and H. A. Spetzler, Transient creep in natural and synthetic, iron-bearing olivine single crystals: Mechanical results and dislocation microstructures, *Tectonophys.*, *235*, 293–315, 1994.

Hess, H. H., History of ocean basins, in *Petrologic Studies*, edited by E. F. Buddington, pp. 599–620, Geol. Soc. Am. Mem., Boulder, Colo., 1962.

Hung, S.-H., and D. W. Forsyth, Modelling anisotropic wave propagation in oceanic inhomogeneous structures using the parallel multidomain pseudo-spectral method, *Geophys. J. Int.*, *133*, 726–740, 1998.

Jaraslow, G. E., G. Hirth, and H. J. B. Dick, Abyssal peridotite mylonites: Implications for grain-size sensitive flow and strain localization in the oceanic lithosphere, *Tectonophys.*, *256*, 17–37, 1996.

Jha, K., E. M. Parmentier, and J. Phipps Morgan, The role of mantle-depletion and melt-retention buoyancy in spreading center segmentation, *Earth Planet Sci Lett.*, *125*, 221–234, 1994.

Kaminski, E., and N. M. Ribe, A kinematic model for recrystallization and texture development in olivine polycrystals, *Earth Planet. Sci. Lett.*, *189*, 253–267, 2001.

Karato, S., Does partial melting reduce the creep strength of the upper mantle?, *Nature*, *319*, 309–310, 1986.

Karato, S., The role of recrystallization in the preferred orientation of olivine, *Phys. Earth Planet. Int.*, *51*, 107–122, 1988.

Karato, S., and P. Wu, Rheology of the upper mantle—A synthesis, *Science*, *260*, 771–778, 1993.

Kelemen, P. B., G. Hirth, N. Shimizu, M. Spiegelman, and H. J. B. Dick, A review of melt migration processes in the adiabatically upwelling mantle beneath oceanic spreading ridges, *Philos. Trans. R. Soc. London Ser. A*, *355*, 283–318, 1997.

Kocks, U. F., Laws for work-hardening and low-temperature creep, *J. Eng. Mater. Technol.*, *98*, 76–85, 1976.

Kocks, U. F., C. N. Tomé, and H.-R. Wenk, *Texture and Anisotropy: Preferred Orientations in Polycrystals and Their Effect on Materials Properties*, Cambridge Univ. Press, New York, 1998.

Kohlstedt, D., Structure, rheology and permeability of partially molten rocks at low melt fractions, in *Mantle Flow and Melt Generation at Mid-Ocean Ridges*, *Geophys. Monogr. Ser.*, vol. 71, edited by J. Phipps Morgan, D. K. Blackman, and J. M. Sinton, pp. 103–122, AGU, Washington, D. C., 1992. (Available at http://www.g-cubed.org).

Komatitsch, D., C. Barnes, and J. Tromp, Simulation of anisotropic wave propagation based upon a spectral element method, *Geophysics*, *65*, 1251–1260, 2000.

Kumazawa, M., The elastic constants of single-crystal orhopyroxene, *J. Geophys. Res.*, *74*, 5973–5980, 1969.

Lebensohn, R. A., and C. N. Tomé, A selfconsistent approach for the simulation of plastic deformation and texture development of polycrystals: Application to zirconium alloys, *Acta Metall. Mater.*, *41*, 2611–2624, 1993.

Mainprice, D., and P. G. Silver, Interpretation of SKS-waves using samples from the subcontinental lithosphere, *Phys. Earth. Planet. Int.*, *78*, 257–280, 1993.

Mainprice, D., G. Barroul, and W. Ben Ismaïl, The seismic anistropy of the Earth's mantle: From single crystal to polycrystal, in *Earth's Deep Interior*, *Geophys. Monogr. Ser.*, vol. 117, pp. 237–264, AGU, Washington, D. C., 2000.

Mathur, K. K., and P. R. Dawson, On modeling the development of crystallographic texture in bulk forming process, *Int. J. Plasticity*, *5*, 67–94, 1989.

Mika, D. P., and P. R. Dawson, Polycrystal plasticity modeling of intracrystalline boundary textures, *Acta Mater.*, *47*, 1355–1369, 1999.

Molinari, A., Extensions of the self consistent tangent model, *Modell. Simul. Mater. Sci. Eng.*, *7*, 683–697, 1999.

Molinari, A., and L. S. Toth, Tuning a selfconsistent viscoplastic model by Finite-Element results, I, Modeling, *Acta Metall. Mater.*, *42*, 2453–2458, 1994.

Molinari, A., G. R. Canova, and S. Ahzi, A selfconsistent approach of the large deformation polycrystal viscoplasticity, *Acta Metall.*, *35*, 2983–2994, 1987.

Nicolas, A., *Structure of Ophiolites and Dynamics of Oceanic Lithosphere*, 367 pp., Kluwer Acad., Norwell, Mass., 1989.

Nishimura, C. E., and D. W. Forsyth, The anisotropic structure of the upper mantle in the Pacific, *Geophys. J. Int.*, *96*, 203–229, 1989.

Ribe, N. M., Seismic anisotropy and mantle flow, *J. Geophys. Res.*, *94*, 4213–4223, 1989.

Ribe, N. M., On the relation between seismic anisotropy and finite strain, *J. Geophys. Res.*, *97*, 8737–8747, 1992.

Rümpker, G., A. Tommasi, and J.-M. Kendall, Numerical simulations of depth-dependent anisotropy and frequency-dependent wave propagation, effects, *J. Geophys. Res.*, *104*, 23,141–23,153, 1999.

Saltzer, R. L., J. B. Gaherty, and T. H. Jordan, How are vertical

shear wave splitting measurements affected by variations in the orientation of azimuthal anistropy with depth?, *Geophys. J. Int.*, *141*, 374–390, 2000.

Sarma, G. B., and P. R. Dawson, Effects of interactions among crystals on the inhomogeneous deformations of polycrystals, *Acta Mater.*, *44*, 1937–1953, 1996.

Savage, M. K., Seismic anisotropy and mantle deformation: What have we learned from shear wave splitting, *Rev. Geophys.*, *37*, 65–106, 1999.

Schulte-Pelkum, V., Mantle structure and anistropy from the particle motion and slowness of compressional body waves, Ph.D. Thesis, Univ. of Calif., San Diego, 2001.

Scott, D. R., Small-scale convection and mantle melting beneath mid-ocean ridges, in *Mantle Flow and Melt Generation at Mid-Ocean Ridges*, *Geophys. Monogr. Ser.*, vol. 71, edited by J. Phipps Morgan, D. K. Blackman, and J. M. Sinton, pp. 327–352, AGU, Washington, D. C., 1992.

Shimamura, H., Anisotropy in the oceanic lithosphere of the Northwestern Pacific basin, *Geophys. J. R. Astron. Soc.*, *76*, 253–260, 1984.

Sileny, J., and J. Plomerova, Inversion of shear-wave splitting parameters to retrieve three-dimensional orientation of anisotropy in continental lithosphere, *Phys. Earth Planet. Int.*, *95*, 277–292, 1996.

Silver, P. G., Seismic anisotropy beneath the continents-probing the depths of geology, *Ann. Rev. Earth Planet. Sci.*, *24*, 385–432, 1996.

Silver, P. G., and W. W. Chan, Shear wave splitting and subcontinental mantle deformation, *J. Geophys. Res.*, *96*, 16,429–16,454, 1991.

Silver, P. G., and M. K. Savage, The interpretation of shear-wave splitting parameters in the presence of two anisotropic layers, *Geophys. J. Int.*, *119*, 949–963, 1994.

Takeshita, T., H.-R. Wenk, A. Molinari, and G. Canova, Simulation of dislocation assisted plastic deformation in olivine polycrystals, in *Deformation Processes in Minerals, Ceramics and Rocks*, edited by D. J. Barber and P. G. Meredith, pp. 365–377, Allen and Unwin, Concord, Mass., 1990.

Takeshita, T., H.-R. Wenk, G. Canova, and A. Molinari, Simulation of dislocation-assisted plastic deformation in olivine polycrystals, in *Deformation Processes in Minerals, Ceramics and Rocks*, pp. 365–377, Unwin Hyman, Boston, Mass., 1999.

Taylor, G. I., Plastic strain in metals, *J. Inst. Met.*, *62*, 307–324, 1938.

Tomé, C. N., Self-consistent polycrystal models: A directional compliance criterion to describe grain interactions, *Modell. Simul. Mater. Sci. Eng.*, *7*, 723–738, 1999.

Tomé, C. N., and G. Canova, Self-consistent modeling of heterogeneous plasticity, in *Texture and Anisotropy*, edited by U. Kocks, C. Tomé, and H.-R. Wenk, pp. 466–511, Cambridge Univ. Press, New York, 1998.

Tommasi, A., Forward modeling of the development of seismic anisotropy in the upper mantle, *Earth Planet. Sci. Lett.*, *160*, 1–13, 1998.

Tommasi, A., D. Mainprice, G. Cannova, and Y. Chastel, Viscoplastic self-consistent equilibrium modeling of olivine lattice preferred orientations: Implications for the upper mantle seismic anisotropy, *J. Geophys. Res.*, *105*, 7893–7908, 2000.

Turcotte, D. L., and J. Phipps Morgan, The physics of magma migration and mantle flow beneath a mid-ocean ridge, in *Mantle Flow and Melt Generation at Mid-Ocean Ridges*, *Geophys. Monogr. Ser.*, vol. 71, edited by J. Phipps Morgan, D. K. Blackman, J. M. Sinton, pp. 155–182, AGU, Washington, D. C., 1992.

Van Houtte, P., On the equivalence of the relaxed Taylor theory and the Bishop-Hill theory for partially constrained plastic deformation of crystals, *Mater. Sci. Eng.*, *55*, 69–77, 1982.

Wenk, H.-R., NATO Advanced Research Workshop on Polyphase Polycrystal Plasticity, *Mater. Sci. Eng. A*, *175*, 277 pp., 1994.

Wenk, H.-R., A voyage through the deformed Earth with the self-consistent model, *Model. Simul. Mater. Sci. Engin.*, *7*, 699–722, 1999.

Wenk, H.-R., and C. N. Tomé, Modeling dynamic recrystallization of olivine aggregates deformed in simple shear, *J. Geophys. Res.*, *104*, 25,513–25,527, 1999.

Wenk, H.-R., K. Bennett, G. R. Canova, and A. Molinari, Modelling plastic deformation of peridotite with the self-consistent theory, *J. Geophys. Res.*, *96*, 8337–8349, 1991.

Wenk, H.-R., G. Canova, Y. Bréchet, and L. Flandin, A deformation-based model for recrystallization of anisotropic materials, *Acta Mater.*, *45*, 3283–3296, 1997.

Wenk, H.-R., P. Dawson, C. Pelkie, and Y. Chastel (Producers), *Texturing of Rocks in the Earth's Mantle: A Convection Model Based on Polycrystal Plasticity* [Movie], 28 min, AGU, Washington, D. C., 1999.

Wolfe, C. J., and S. C. Solomon, Shear-wave splitting and implication for mantle flow beneath the MELT region of the East pacific Rise, *Science*, *280*, 1230–1232, 1998.

Zhang, S., and S. Karato, Lattice preferred orientation of olivine deformed in simple shear, *Nature*, *375*, 774–777, 1995.

Zhang, S., S. Karato, J. Fitz Gerald, U. H. Faul, and Y. Zhou, Simple shear deformation of olivine aggregates, *Tectonophysics*, *316*, 133–152, 2000.